Geophysical Journal International

Geophys. J. Int. (2023) **233,** 2142–2154
Advance Access publication 2023 February 09
GJI Seismology

https://doi.org/10.1093/gji/ggad055

Warm versus cold crust in the Tien Shan orogenic belt revealed by seismic Lg attenuation tomography

Xiao Ma,[1,2] Lian-Feng Zhao ,[1,3] Xiao-Bi Xie,[4] Xu Chang[1] and Zhen-Xing Yao[1]

[1] *Institute of Geology and Geophysics, Chinese Academy of Sciences, Key Laboratory of Earth and Planetary Physics, Beijing* 100045, *China.*
E-mail: zhaolf@mail.iggcas.ac.cn
[2] *University of Chinese Academy of Sciences, College of Earth and Planetary Sciences, Beijing* 101408, *China*
[3] *Institute of Geology and Geophysics, Chinese Academy of Sciences, Heilongjiang Mohe Observatory of Geophysics, Beijing* 100045, *China*
[4] *University of California at Santa Cruz, Institute of Geophysics and Planetary Physics, Santa Cruz, CA* 95064, *USA*

Accepted 2023 February 5. Received 2023 January 29; in original form 2022 August 15

SUMMERY

Due to the far-field effect of the India–Eurasia collision, the Tien Shan orogenic belt has been undergoing reactivation and modification. Two end-member models of the geodynamic mechanisms are (1) surface uplift due to crustal shortening caused by lithospheric compression and (2) mountain formation resulting from thermal upwelling of asthenospheric mantle materials generated by lithospheric subduction. However, the topography along the Tien Shan orogenic belt changes significantly, and the deep structure and dynamic process are quite different beneath the Tien Shan orogenic belt from both geological and geophysical observations. Therefore, the reactivation and modification of the Tien Shan orogenic belt are likely influenced by both geodynamic mechanisms, which also generate various thermal anomalies in the crust. Seismic Lg-wave attenuation is very sensitive to crustal material composition and status and can point to the presence of partial melting within the crust resulting from mantle upwelling. In this study, we develop a high-resolution Lg-wave attenuation model between 0.05 and 10.0 Hz in Northwest China and use lateral attenuation variations to infer thermal structures in the crust. The central Tien Shan is characterized by prominent low-Q_{Lg} anomalies, whereas relatively high-Q_{Lg} distributions are imaged beneath the eastern and western Tien Shan. The surface uplift and crustal deformation are mostly related to the upwelling of hot mantle materials in the central Tien Shan and are likely induced by lithospheric compression in the eastern and western Tien Shan. However, low-Q anomalies are observed in the junction between the Pamir Plateau and western Tien Shan, indicating that the uplift in the south of the western Tien Shan is related to thermal subduction-induced upwelling and intrusion into the crust due to the collision between the Indian and Eurasian plates. The Kazakh Shield, characterized by pronounced high-Q_{Lg} values, is likely a cold and hard terrane, and hence blocks the far-field effect of the India–Eurasia collision.

Key words: Guided waves; Seismic attenuation; Seismic tomography; Crustal structure; Rheology: crust and lithosphere.

1 INTRODUCTION

Northwest China and its surrounding areas are composed of several major geological blocks: the Kazakh Shield, Altai Mountains, Junggar Basin, Tien Shan orogenic belt, Turpan-Hami Basin, Tarim Basin and Pamir Plateau, from north to south (Fig. 1). Geographically, the Tien Shan orogenic belt, located at the southwestern margin of the Central Asian Orogenic Belt (CAOB; Sengor *et al.* 1993; Xiao *et al.* 2013), is one of the most active and youngest intracontinental orogenic belts in the world with intense seismic and tectonic activity, making it an ideal natural laboratory to study the crustal deformation and tectonic evolution mechanisms of an intracontinental orogenic belt (Li *et al.* 2009; Zhou *et al.* 2011; England & Molnar 2015; Lü & Lei 2018).

The Tien Shan orogenic belt is situated more than 1500 km from the India–Eurasia collision, and extends approximately 2500 km in the east–west direction with a width of up to 400 km in the north–south direction in its western part (e.g. Burtman 2015; England & Molnar 2015; Yu *et al.* 2017). This orogenic belt is composed of several parallel ranges and intermountain basins oriented nearly east–west and surrounded by several stable blocks, such as the Junggar Basin and Kazakh Shield to the north and the Tarim Basin to

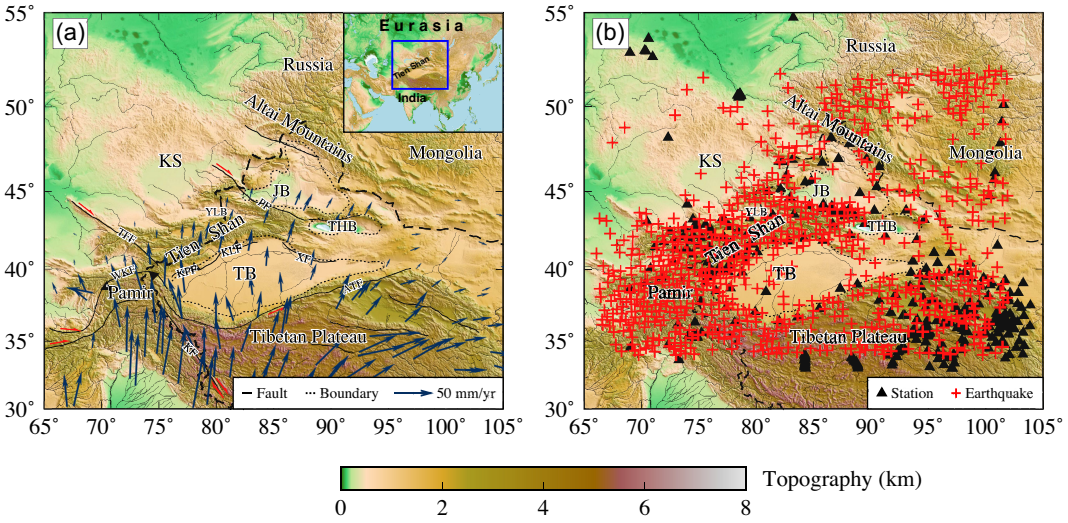

Figure 1. Topographic map of the study region with major tectonic boundaries and faults. (a) Velocities of GPS sites relative to Eurasia (Kreemer *et al.* 2014). The thick black solid lines mark the major faults. The thin dashed lines mark the outlines of the major sedimentary basins. The inset map at the top right shows the Eurasia continent, in which the blue rectangle indicate the location of the study region. KS, Kazakh Shield; JB, Junggar Basin; THB, Turpan-Hami Basin; TB, Tarim Basin; YLB, Yi Li Basin; PF, Poluokelu fault; TFF, Talas-Fergana fault; WKF, west of Kunlun fault; KF, Karakoram fault; KLF, Kuerle fault; KPF, Keping fault; XF, Xingdi fault; ATF, Altyn Tagh fault. (b) Distributions of seismic stations (black triangles) and earthquakes (red crosses) used in this study.

the south. In general, the Tien Shan orogenic belt can be divided into three segments from west to east: the western, central, and eastern Tien Shan (WTS, CTS and ETS, respectively; e.g. Lei 2011; Zhou & Lei 2015). The WTS and CTS are separated by the NW–SE dextral strike-slip Talas-Fergana fault, while the WTS is connected to the arc-sharped Pamir Plateau. The boundary between the central and eastern parts is defined at a geographic longitude of approximately 80°E, while the ETS is generally located in Northwest China (e.g. Lei 2011; Zhou *et al.* 2011; Burtman 2015).

The Tien Shan orogenic belt is originally formed in the late Palaeozoic and is associated with the closure of the Palaeo-Asian Ocean and the accretion of continental blocks and island arcs (e.g. Burtman 1975; Windley *et al.* 1990). Several multistage magmatic episodes are identified from the late Cambrian to late Permian based on zircon U/Pb dating (De Grave *et al.* 2011). In the Tien Shan orogenic belt, there are lots of intracontinental faults characterized by active periods during the Triassic and Jurassic and remained stable during the Cretaceous and early Tertiary (Omuralieva *et al.* 2009). However, the far-field effect of the India–Eurasia collision since approximately 50 Ma makes the modern Tien Shan rejuvenated in the late Cenozoic (e.g. Molnar & Tapponnier 1975; Yin *et al.* 1998; Kaban & Yuanda 2014). The tectonic activity continues to the present day in the Tien Shan orogenic belt based on current intracontinental seismicity and complex Cenozoic tectonics (e.g. Chen *et al.* 1997; Molnar & Ghose 2000).

The Tien Shan orogenic belt is undergoing significant north–south shortening with the surface velocity decreasing gradually from west to east, as evidenced by the GPS velocities which vary from ∼20 mm yr^{-1} in WTS to 6–9 mm yr^{-1} in EST (Fig. 1; Abdrakhmatov *et al.* 1996; Reigber *et al.* 2001; Kreemer *et al.* 2014). Such a shortening rate is closely related to the rigid Tarim Craton, which transfers compressional stresses from the India–Eurasia collision to the Tien Shan orogenic belt (e.g. Molnar & Tapponnier 1975; Abdrakhmatov *et al.* 1996; Craig *et al.* 2012). The crustal thickness is estimated to be approximately 60 km in Tien Shan, which is nearly 20 km thicker than those of the surrounding basins (e.g. Vinnik *et al.* 2004, 2006; Stolk *et al.* 2013). The strike-parallel fast polarization direction was observed along the Tien Shan orogenic belt (Chen *et al.* 2005; Li *et al.* 2010). Therefore, the ongoing north–south shortening leads to vertically coherent deformation of the lithosphere and suggests that the crust and lithospheric mantle are mechanically coupled (Cherie *et al.* 2016). There are mainly two lithospheric deformation mechanisms to control crustal shortening and uplift in the Tien Shan orogenic belt: the lithospheric compression accompanied by potential delamination of the Tien Shan lithosphere (e.g. Kosarev *et al.* 1993), and thermal upwelling triggered by two-way underthrusting of the Kazakh Shield and Tarim Basin (Xu *et al.* 2002; Lei & Zhao 2007; Koulakov 2011; Sychev *et al.* 2018). Beneath the CTS, two-way underthrusting of the Tarim and Kazakh Shield lithosphere can be described by northward- and southward-dipping high-velocity anomalies based on seismic tomography (Xu *et al.* 2002; Lei & Zhao 2007; Li *et al.* 2009; Zabelina *et al.* 2013). The subduction lithosphere extends down to the mantle transition zone in terms of high-velocity root-like anomalies beneath the CTS (Xu *et al.* 2002; Lei & Zhao 2007; Koulakov 2011; Zabelina *et al.* 2013). Also, the thick mantle transition zone reveals the possible presence of a cold lithospheric segment in this region (Tian *et al.* 2010; Yu *et al.* 2017), which may lead to the upwelling of asthenospheric thermal materials. Thermal upwelling may thin and weaken the Tien Shan mantle lithosphere, resulting in the uplift of the Tien Shan orogenic belt (Kumar *et al.* 2005). Prominent low-velocity anomalies were observed in the uppermost mantle and lower crust beneath the Tien Shan orogenic belt, so that thermal upwelling of asthenospheric materials may have intruded or heated the crust in this region (Xu *et al.* 2002; Xu *et al.* 2007; Omuralieva *et al.* 2009; Lei 2011; Gilligan *et al.* 2014; Li *et al.* 2016b; Sychev *et al.* 2018). However, the ETS uplift is suggested to attribute to lithospheric compression, considering that the convergent effect between the Tarim and Junggar Basin lithospheres consequently prevents asthenospheric upwelling (Lü *et al.* 2019). Moreover, according to the Pn anisotropy results (Zhou & Lei 2015), the CTS and ETS show good consistency in anisotropy and lateral heterogeneity but they are different from the WTS, reflecting the dominant controlling factor in the orogenic process of the WTS is different.

Therefore, alongside complex geodynamic processes, the deep hot upwelling modifies the Tien Shan orogenic belt but with significantly different degrees along the mountain strike, in terms of both seismic velocities and topographic features. The thermal structure in the crust, which can be constrained by seismic attenuation, plays a key role in investigating thermodynamic processes of tectonic evolution in the Tien Shan orogenic belt (e.g. Aki 1980; Boyd *et al.* 2004; Bürgmann & Dresen 2008). Seismic Lg wave can be considered as superposed higher-mode surface waves or multiple supercritical *S*-wave reflections propagating in the crustal waveguide (e.g. Bouchon 1982; Xie 2002). The quality factor, $Q_{\rm Lg}$, is generally used to describe the decay of Lg wave in a medium, with low $Q_{\rm Lg}$ values representing strong attenuation and high $Q_{\rm Lg}$ values indicating weak attenuation. Strong crustal deformation generally occurs in active tectonic regions, such as the Tibetan Plateau, the Iranian Plateau, and the western American, where the crust is characterized by strong Lg attenuation or low-$Q_{\rm Lg}$ (e.g. Fan & Lay 2002; Xie *et al.* 2006; Zhao *et al.* 2013a; Zhao & Xie 2016; Gallegos *et al.* 2017). In contrast, the stable shields usually feature less deformation and weak attenuation or high $Q_{\rm Lg}$, such as those in eastern North America, eastern China and Australia (Zhao *et al.* 2010, 2013b; Wei *et al.* 2017; Zhao & Mousavi 2018). Strong Lg-wave attenuation variations and significant lateral heterogeneities were observed in the Tien Shan orogenic belt (Taylor *et al.* 2003; Phillips *et al.* 2005; Zhou *et al.* 2011). Taylor *et al.* (2003) used the Bayesian method to investigate the Lg attenuation in East Asia and obtained the Q_0 map (Q at 1.0 Hz) which gave Q_0 values ranging between 300 and 450 in the Tien Shan orogenic belt. The southern WTS and CTS are characterized by low Q_0 values (∼300), whereas the surrounding stable regions show high Q_0 values, such as those beneath the Kazakhstan shield (>700) and Tarim Basin (∼450). Phillips *et al.* (2005) obtained a $Q_{\rm Lg}$ model in central and eastern Asia by using amplitude ratio techniques and showed a strong attenuation in the CTS (Q_0 ∼250) and weaker attenuation in the Tarim Basin (Q_0∼500). Zhou *et al.* (2011) presented a frequency-dependent $Q_{\rm Lg}$ model (0.5–5.0 Hz) and showed that the Q_0 of the CTS is 251, which is obviously lower than that of the Tarim Basin (∼474). Most of these studies only provided Q_0 values with relatively larger uncertainties due to the limited data used. Because the variation in $Q_{\rm Lg}$ with frequency is not in accordance with power-law models over a wide frequency range (Pasyanos *et al.* 2009; Zhao *et al.* 2010), a $Q_{\rm Lg}$ model with only Q_0 values or certain frequency band $Q_{\rm Lg}$ may not describe the attenuation characteristics of the crust. For example, the frequency band of strong attenuation caused by thick sediments is possibly 0.2–1.0 Hz (Mitchell & Hwang 1987), whereas the possible frequency band of low $Q_{\rm Lg}$ values generated by tectonic fractures in the upper crust or near-surface hydrothermal fluid is 2.0–10.0 Hz (Zhao *et al.* 2013a). In this study, we use a large number of high-quality broad-band digital seismic records to develop a broad-band Lg attenuation model in Northwest China and its surrounding areas, to constrain the thermal structures of the crust beneath the Tien Shan orogenic belt, and to improve our understanding to the geodynamic processes of reactivation and modification in the Tien Shan orogenic belt.

2 DATA AND METHODS

In this study, we collected 71 679 broad-band vertical component digital seismograms from 711 crustal earthquakes that occurred in Northwest China and its surrounding areas between November 1994 and August 2017. Seismograms were collected from 383 seismic stations, including 128 stations from the China Earthquake Network Center (CENC) and 255 stations from the Incorporated Research Institutions for Seismology (IRIS; Fig. 1). The selection of earthquakes followed these criteria: to ensure they are crustal events, the focal depths are shallower than the Moho depth from CRUST1.0 (Laske *et al.* 2013); the epicentral distances are between 200 and 3000 km and clear Lg waveforms can be observed; the magnitude range is between $m_{\rm b}$ 4.2 and 6.2 to improve the signal-to-noise ratios and avoid the complex rupture processes of large earthquakes.

To obtain the spectral amplitudes of the Lg wave, we conducted data pre-processing for all available Lg waveforms (Xie & Mitchell 1990; Zhao *et al.* 2010, 2013b; Zhao & Xie 2016). For the Lg amplitude measurement, the Lg-wave group velocity is a vital parameter to correctly identify and pick the Lg phase in the waveform data. Considering that the group velocity can be affected by the regional crustal structure and uncertainties introduced by the origin times, event locations, and focal depth, we set a 0.6 km s^{-1} group velocity window shifting between 3.8 and 2.6 km s^{-1} to scan the waveforms and selected the Lg sampling windows with maximum energy arrival. Most Lg group velocity windows are approximately 3.6–3.0 km s^{-1}, which is also a typical range for Lg-wave observations in other regions (Pasyanos *et al.* 2009; Zhao *et al.* 2010, 2013a,b; Zhao & Xie 2016). Next, we used both pre-event and pre-phase noise for data quality control (QC) of the obtained Lg-wave spectra. The Pn wave appears as the first arrival at regional phase distances. Thus, pre-Pn noise and pre-Lg noise were picked before the first Pn-wave arrival and immediately before the Lg phase for pre-event and pre-phase noise, respectively, with the same length as the Lg waves. A fast Fourier transform was performed for the Lg-wave phase, pre-Pn and pre-Lg noise, and we sampled the spectral amplitudes at 58 reference frequencies distributed evenly between 0.05 and 10.0 Hz on a logarithmic scale. Then, we conducted noise correction for data quality control. The signal-to-noise ratio (SNR) between the power spectra of the raw Lg phase and noise series can be calculated as $\mathrm{SNR}\,(f) = A_{origin}(f)/A_{noise}(f)$. The pre-Pn noise is usually a random and stationary signal. On a typical quiet station, its amplitude should be lower than the Lg signal. Therefore, we chose a pre-Pn SNR threshold of 2.0 to QC the Lg data. On the other hand, the pre-Lg noise is mainly composed of P- and Sn-wave codas. They are not stationary phases. As scattering waves, they usually decay with elapsed time and are strongly frequency dependent. The spectral amplitude of the pre-Lg noise in its sampling window could be comparable to the Lg-wave amplitude, although its actual contribution to the Lg amplitude is likely smaller due to its continuously decaying after entering the Lg-wave window. Considering the above situation, a lower pre-Lg SNR threshold of 1.0 is used to QC the Lg data. The P and Sn coda waves are highly unstable and decay. If trying to correct its effect, a frequency-dependent coda decaying model is required, but it is hard to obtain such a model using the current data set. Furthermore, the P- and Sn-coda can be composed of much *S*-wave energy converted from other wave types (e.g. Kennett 1986; Xie & Lay 1994). Traditionally, when entering into the Lg-wave window, this energy will be countered as Lg-wave energy. Therefore, to avoid introducing additional errors, we did not conduct correction for the effect of pre-Lg noise. Thus, we eliminated relatively low-quality data by introducing a pre-Pn SNR threshold of 2.0 and removed the data that was mainly composed of the Sn coda by setting a pre-Lg SNR threshold of 1.0. In addition, we assume that the recorded wave trains in the Lg-wave window represent the superposition of the Lg wave and background noise and that the two are uncorrelated. The pre-Pn noise correction was also achieved by applying $\mathrm{A}^2_{\rm Sig}(f) = \mathrm{A}^2_{\rm Obs}(f) - \mathrm{A}^2_{\rm noi}(f)$,

where $A(f)$ is the spectral amplitude and the subscripts sig, obs and noi denote the amplitudes of the true signal, observed data, and pre-event noise, respectively. As an example, Fig. 2 illustrates this data pre-processing for event 2014/12/06 recorded at station WMQ, where Figs 2(a) and (b) are velocity records after removing the instrument response and the envelope of 0.5–5.0 Hz filtered waveforms, respectively, and the grey parts are the group velocity windows in which 10 per cent duration intervals were added both before and after windows and cosine tapers were applied on the extended portions. Figs 2(c)–(e) show windowed wave trains for the Lg wave, pre-Pn and pre-Lg noise series; Fig. 2(f) shows 58 discrete amplitude spectra calculated between 0.05 and 10.0 Hz for the Lg wave and noise; and Figs 2(g)–(h) show the noise correction and Lg-wave spectrum after denoising. After batch processing all of the regional waveforms, we obtained the source-station (single-station) amplitudes at 58 individual frequencies between 0.05 and 10.0 Hz. Then, we extracted the interstation (two-station) data for 58 individual frequencies from a single-station data set by following Zhao *et al.* (2013b). The two-station data can produce accurate Q estimation by eliminating the trade-off between the source term and attenuation, and the single-station data can provide fine resolution due to its dense ray path coverage; thus, both types of data were used in the joint inversion for the Q_{Lg} value and the source function frequency by frequency.

We used the tomographic method proposed by Zhao *et al.* (2010, 2013b) to jointly invert source excitation and regional Q based on both the single- and two-station data. This method has been successfully applied in Northeast China (Zhao *et al.* 2010), North China (Zhao *et al.* 2013b), the Tibetan Plateau (Zhao *et al.* 2013a; He *et al.* 2021), Southeast Asia (Luo *et al.* 2021), the Middle East (Zhao & Xie 2016), the Australian continent (Wei *et al.* 2017) and eastern North America (Zhao & Mousavi 2018) to study crustal Lg attenuation, which reveals the relationship between Q_{Lg} variations and regional tectonics. We set the unit source function as the initial source model and obtained a low-resolution Q model from two-station data as the initial attenuation model. In each iteration, we combined both single- and two-station data to solve the perturbations of Q and the source term by minimizing the residuals between the observed and synthesized Lg-wave spectra for each individual frequency. These perturbations were used to update the Q model and source function until satisfactory convergence was obtained in the iterative process. In addition, we assumed that the sum of all the changes in the site response was zero and determined the site response for each station given the inverted source and attenuation by pushing the unsolved residuals into the site term. Thus, we obtained the frequency-dependent Q values, source functions, and site response by inverting independently for individual frequencies. Fig. 3 shows residual distributions for the initial and final models at 0.5, 1.0, 2.0 and 3.0 Hz. After the inversion, the data residuals are largely reduced and their distribution tends to be a Gaussian function with a zero mean and a much smaller standard deviation (Fig. 3). For example, at 1.0 Hz, the rms residual decreased from 2.36 to 0.90, the mean value from 1.50 to 0.02 and the standard deviation from 1.81 to 0.90. This implies a better data fit after the inversion. The remaining unsolved residuals may result from complex source processes, site responses and other random effects, which are neglected in our joint inversion (e.g. Zhao & Mousavi 2018).

The resolution of inversion results with current data sets is usually estimated by performing checkerboard tests. We first created a constant background Q model superimposing 7 per cent checkerboard-shaped positive and negative perturbations (e.g. Zelt 1998; Zhou *et al.* 2011, 2013a; Liu *et al.* 2014). Next, we used the same real data set of the source, stations and ray paths to generate a synthetic Lg spectrum data set at each frequency. To simulate the real data, 5 per cent rms random noise was added to the synthetic spectra (e.g. Zhao *et al.* 2010, 2013a; He *et al.* 2021). To estimate the resolution, the synthetic data were inverted and the resulting Q_{Lg} was compared with the original checkerboard model. Fig. 4 illustrates the raypath coverages and checkerboard resolution tests at 0.5, 1.0, 2.0 and 3.0 Hz, respectively. The grey rays are for the single-station data and the blue rays are for two-station data. The spatial resolution also varies with frequency as the ray path coverage varies. Apparently, ray coverage is dense in most areas but relatively sparse in the northwestern part. It is clear that in the major tectonic units of the study area, such as the Tien Shan orogenic belt, the Tarim Basin, the Junggar Basin and the northeastern margin of the Pamir Plateau, the checkerboard test is well resolved and the spatial resolution approaches $1^\circ \times 1^\circ$ or higher. However, in the northwestern part of the study region, such as the Kazakh Shield, the resolved checkerboard model is not as good as those in other regions because of the sparse ray path coverage.

3 RESULTS

Based on the above-mentioned data set and inversion methods, we obtained a broad-band crustal Lg-wave attenuation model of Northwest China and its surrounding areas at 58 individual frequencies between 0.05 and 10.0 Hz.

3.1 Q_{Lg} maps at individual frequencies

The Q_{Lg} images at frequencies of 0.5, 1.0, 2.0 and 3.0 Hz are selected for analysis, as shown in Fig. 4. Overall, the Q_{Lg} values at high frequencies are higher than the values at low frequencies, and the patterns of the low-Q_{Lg} (high attenuation with red color) and high-Q_{Lg} (low attenuation with blue colour) distributions at different frequencies show similar large-scale lateral variations, demonstrating the stability and reliability of the tomographic results. The lateral variation indicates significant lateral heterogeneities within the crust of the study region, which is quite consistent with the regional geological tectonics. Notably, the tectonically active regions, such as the central part of the Tien Shan orogenic belt and the Pamir Plateau, where GPS velocities reveal intense deformation, are characterized by low-Q_{Lg} anomalies that are higher than those of other blocks, corresponding to relatively high surface heat flows between 60 and 70 mW m^{-2} (from International Heat Flow Commission, IHFC; Fuch *et al.* 2021). In contrast, the Tarim Basin, known as a stable craton (Xiao *et al.* 2013), is characterized by relatively weak attenuation at all frequencies, corresponding to relatively low heat flow values between ∼40 and 50 mW m^{-2}. Besides, the Junggar Basin, consisting of trapped oceanic crust formed in the Paleozoic (Xiao *et al.* 2013), is characterized by low values at low frequencies, consistent with low-velocity anomalies detected by Guo *et al.* (2006), where relatively low heat flow values are between ∼40 and 50 mW m^{-2} and sediments are approximately over 10 km thick (Stolk *et al.* 2013). The Kazakh Shield, characterized by pronounced high Q_{Lg} values, is featured by rigid, weakly deformed crust and a cold stable cratonic lithosphere. The Q_{Lg} distribution at 1.0 Hz (Q_0) is comparable with previously published Lg attenuation models with similar dominant features of crustal attenuation, but our result shows higher resolution and better ray paths coverage (Taylor *et al.* 2003; Phillips *et al.* 2005; Zhou *et al.* 2011). An average Q_0 of 262 is very close to 251 obtained by Zhou *et al.* (2011) in the CTS

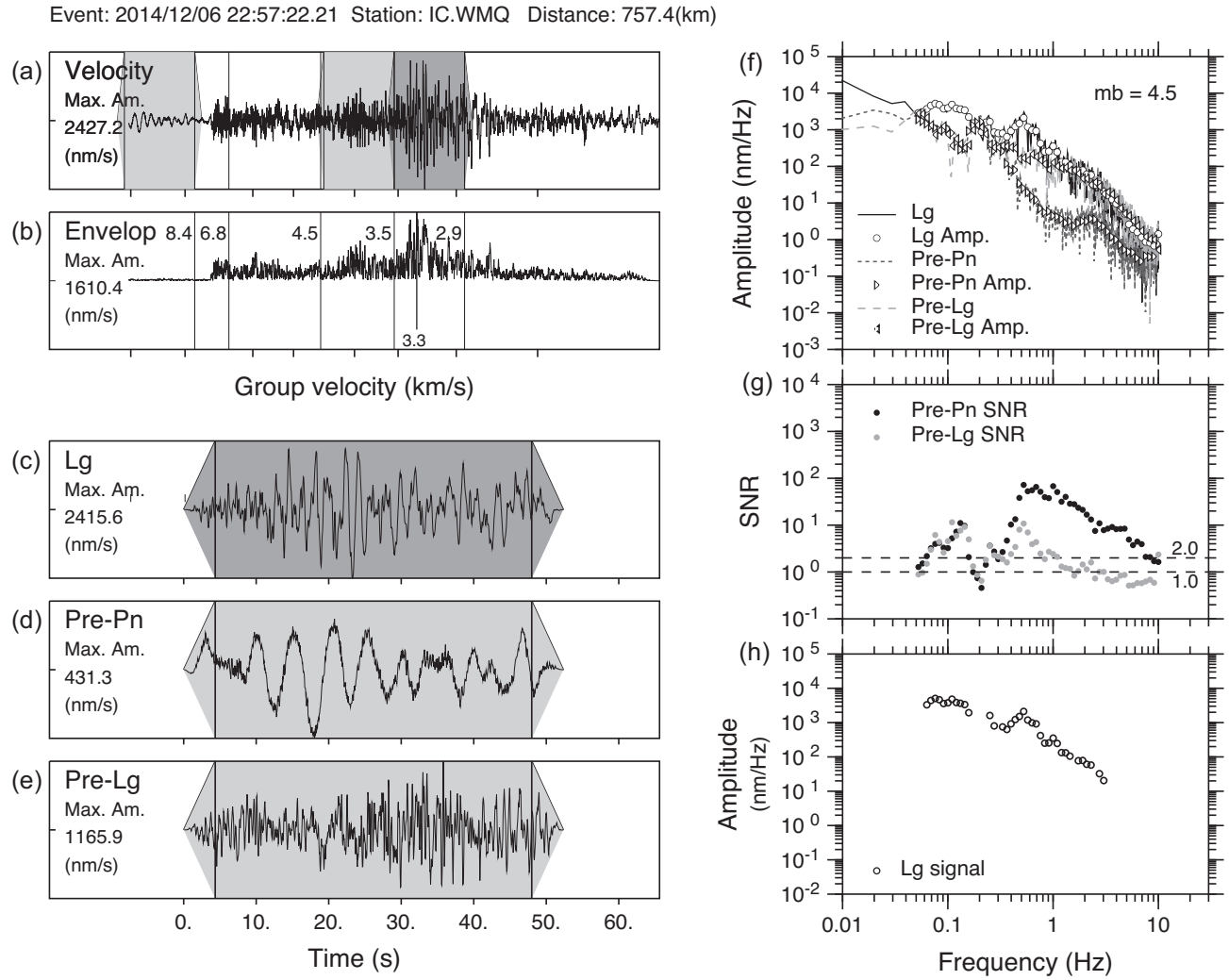

Figure 2. Data pre-processing procedure for a sample Lg waveform. (a) velocity record after removed the instrument response; (b) envelope of 0.5–5.0 Hz filtered waveform for locating the maximum energy arrival and Lg sampling window; (c–e) windowed Lg phase, and pre-Pn and pre-Lg noises; (f) amplitude spectra of pre-Pn noise (dotted line), pre-Lg noise (dashed line) and Lg wave (solid line). The circles and triangles represent the sampled amplitudes at frequencies log evenly distributed between 0.05 and 10.0 Hz. (g) Signal-to-noise ratios and (h) accepted Lg-wave spectral data. Note that data points with their SNR below the thresholds were dropped.

(Table 1). The average Q_0 value of 544 in the Tarim Basin is also in accordance with those obtained by Zhou *et al.* (2011) and Phillips *et al.* (2005). However, there are certain differences in some parts of the study area. For example, Zhou *et al.* (2011) observed weaker attenuation in the ETS and stronger attenuation on the margin of the Junggar Basin than ours. These biases may result from differences in data coverage, inversion resolution, or constraints among individual studies.

3.2 Frequency cross-sections of the Lg attenuation

Using the frequency cross-sections of Q_{Lg} maps, we explore the relationships between the frequency dependence of crustal Lg-wave attenuation and regional geological structures. Six north–south cross-sections for Q_{Lg} versus frequency along selected longitudes are illustrated in Fig. 5. In each panel, the upper part compares the surface topography with main faults, seismicity, and Moho depths from CRUST1.0 (Laske *et al.* 2013), and the lower part shows Q_{Lg} versus frequency. As shown in Figs 5(a)–(c), the profiles traverse the Pamir Plateau, WTS, Tarim Basin, CTS and Kazakh Shield, exhibiting apparent Q_{Lg} variations at the junction of these geo-blocks. The Kazakh Shield is a stable continent with high Q_{Lg} values, whereas significantly low-Q_{Lg} anomalies are observed in the crust of the Pamir, WTS and CTS. Strong attenuation contrasts across the Talas-Fergana fault may be spatially correlated with the boundary between the WTS and CTS. Several strong earthquakes have occurred mainly on the Pamir Plateau and in the Tien Shan (Zhou *et al.* 2011; Zhou & Lei 2015). The seismic activity is very intense in the interior or on the margins of low-Q_{Lg} regions, such as the Pamir and WTS, and the southern and northern margins of the CTS. The locations of historical earthquakes show a certain relation with the distribution of Q_{Lg}. As shown in Figs 5(d)–(f), profiles that pass through the Tarim Basin, CTS, ETS, Junggar Basin and Kazakh Shield reveal apparent low-Q_{Lg} anomalies beneath the CTS, whereas the stable continent blocks, including the Tarim Basin and Kazakh Shield, have higher Q_{Lg} values. The block boundaries of the Junggar Basin, Tarim Basin and Kazakh Shield with the Tien Shan Mountains exhibit sharp Q_{Lg} variations. Along the entire Tien

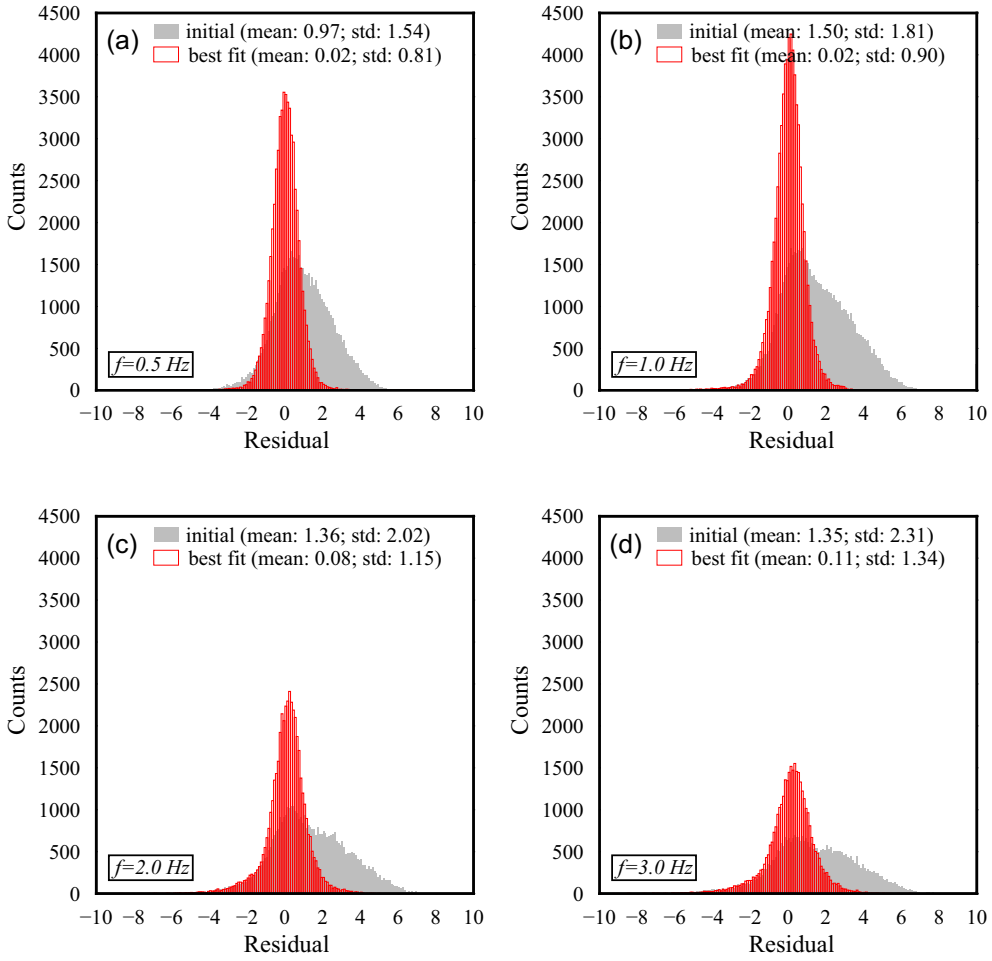

Figure 3. Histograms of the Lg spectral amplitude misfit before (solid grey) and after (open red) inversions, with (a) 0.5, (b) 1.0, (c) 2.0 and (d) 3.0 Hz, respectively.

Shan orogenic belt, the Q_{Lg} values of the CTS appear to be much lower than the Q_{Lg} values beneath the WTS and ETS, which reveals that the CTS is more tectonically active and possibly exhibits widespread partial melting in the crust. On the other hand, the Pamir Plateau has low Q_{Lg} at frequencies lower than approximately 0.3 Hz (Figs 5a and b), and analogous cases can also be found for the Tarim and Junggar Basin (Figs 5b–f). These regions feature either thick sediments or junctions between flatlands and surrounding mountains, which lead to remarkable scattering of Lg waves (Wu *et al.* 2007; Ma *et al.* 2021).

3.3 Broad-band Q_{Lg} images

The Q_{Lg} variations exhibit strong correlations with both frequency and geological structures. In this study, we conducted the Lg-wave attenuation tomography independently at 58 discrete frequencies so that we can investigate the frequency dependency of Lg-wave attenuation, which is a robust quantity to characterize different geological formations (Zhao *et al.* 2010, 2013a,b; Zhao & Xie 2016). The average Q_{Lg} was obtained in statistics for each block, and hence the frequency dependence of the Q_{Lg} can be estimated, such as Q_{Lg} values in the Tarim Basin, Kazakh Shield and Tien Shan block, as shown in Figs 6(a)–(c). In the frequency band between 0.2 and 2.0 Hz, the Q_{Lg} values for the three selected geological blocks follow similar trends: Q_{Lg} gradually increases with increasing frequency, whereas the Q_{Lg} of the Tien Shan block is lower with larger scatters, which may reflect the intensity of tectonic activity in different blocks. Because of the scattering attenuation, the interpretation of Q_{Lg} based on a single frequency may be biased. Choosing the appropriate frequency band to calculate the broad-band Q_{Lg} model can better distinguish the inherent attenuation characteristics of different geological blocks. Thus, we summarized the average Q_{Lg} versus frequency relations for all geological blocks in the region (Fig. 6d) with their results also listed in Table 1 and found that in the frequency band between 0.2 and 2.0 Hz (shaded area in Fig. 6d), the behaviors of Q_{Lg} for these selected blocks follow similar trends and that this band can distinguish the attenuation characteristics of different geological blocks more efficiently than other frequency bands. We further calculated the average Q_{Lg} on a logarithmic scale between 0.2 and 2.0 Hz and obtained the broad-band Q_{Lg} (0.2–2.0 Hz) image for Northwest China and surrounding areas. Similar features can also be found in the broad-band Q_{Lg} map compared with the Q_0 distribution (Fig. 4d). For example, strong Lg-wave attenuation is observed beneath the Tien Shan orogenic belt and the northeastern margin of the Pamir Plateau, whereas the adjacent blocks such as the Tarim Basin and Kazakh Shield show relatively weak attenuation.

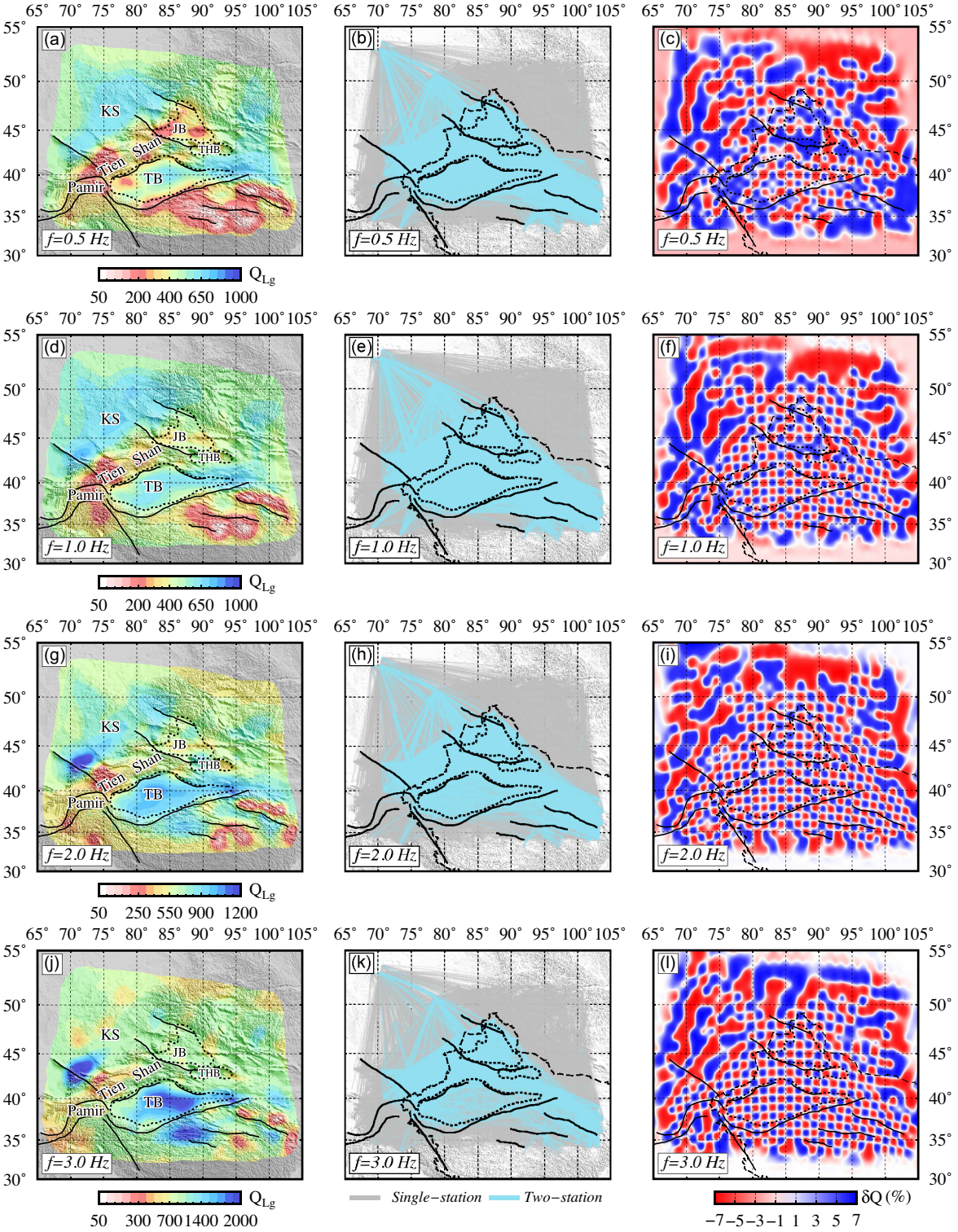

Figure 4. Selected Q_{Lg} maps (left-hand panel), ray path coverage (center panel) and checkboard resolution analysis (right-hand panel) at 0.5 Hz (a–c), 1.0 Hz (d–f), 2.0 Hz (g–i) and 3.0 Hz (j–l). Note that the Q_{Lg} maps at different frequencies use different colour scales. The grey and blue rays are for single-station and two-station data, respectively. The reconstructed checkerboard resolution is 1.0° × 1.0°.

Table 1. Lg Q for individual geological blocks.

Block name	Abbr.	Lg-wave Q model		CRUST1.0 model[a]		IHFC[b]
		Q_0 (1 Hz Q)	Q (0.2–2.0 Hz)	Crustal thickness (km)	Sediment thickness (km)	Heat flow (mW m^{-2})
Tien Shan	TS	362 (308–426)	392 (320–481)	51.0 ± 3.8	0.5 ± 0.9	62.5 ± 21.7
Western Tien Shan	WTS	415 (364–473)	437 (376–509)	47.7 ± 4.9	1.9 ± 2.7	63.2 ± 22.6
Central Tien Shan	CTS	262 (195–365)	275 (212–386)	52.6 ± 2.2	0.4 ± 0.6	63.6 ± 25.2
Eastern Tien Shan	ETS	404 (375–436)	442 (383–512)	50.4 ± 3.6	0.5 ± 0.7	72.1 ± 44.0
Tarim Basin	TB	544 (501–591)	588 (496–697)	46.0 ± 2.6	4.3 ± 2.4	44.8 ± 9.2
Junggar Basin	JB	394 (352–442)	408 (331–503)	44.3 ± 2.2	2.8 ± 2.4	43.0 ± 6.9
Kazakh Shield	KS	590 (549–633)	610 (548–679)	45.4 ± 3.4	0.1 ± 0.2	42.7 ± 11.6

[a]From Laske *et al.* (2013).
[b]IHFC, the International Heat Flow Commission.

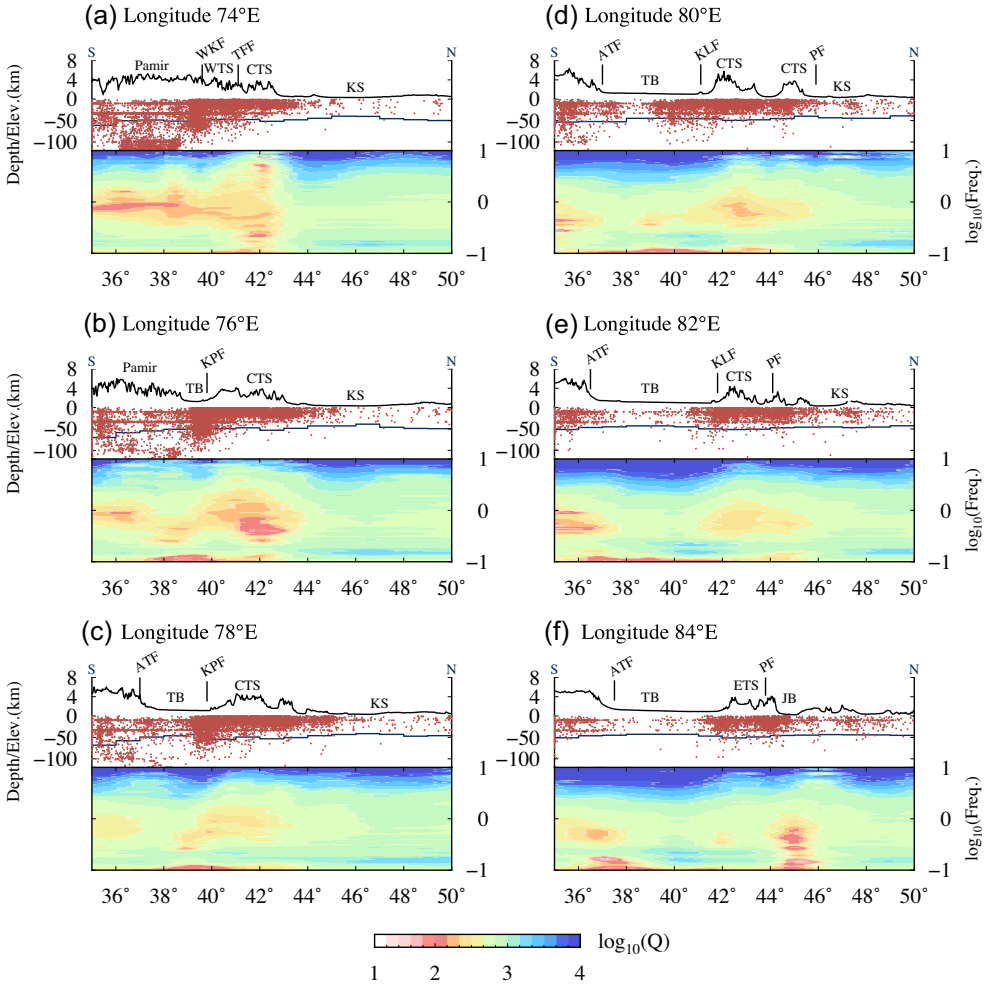

Figure 5. Cross-sections of broad-band Q_{Lg}, with (a)–(f) are along longitudes 74°E, 76°E, 78°E, 80°E, 82°E and 84°E, respectively. In each panel, the topographic elevation, seismicity and Moho depth are shown in the upper part to compare with Q_{Lg}. Red dots denote earthquakes along the profile with magnitudes greater than 2.5 and occurred between 1994 and 2018, collected from the International Seismological Center (ISC). The abbreviations of geological blocks and major faults are labelled, as defined in Fig. 1.

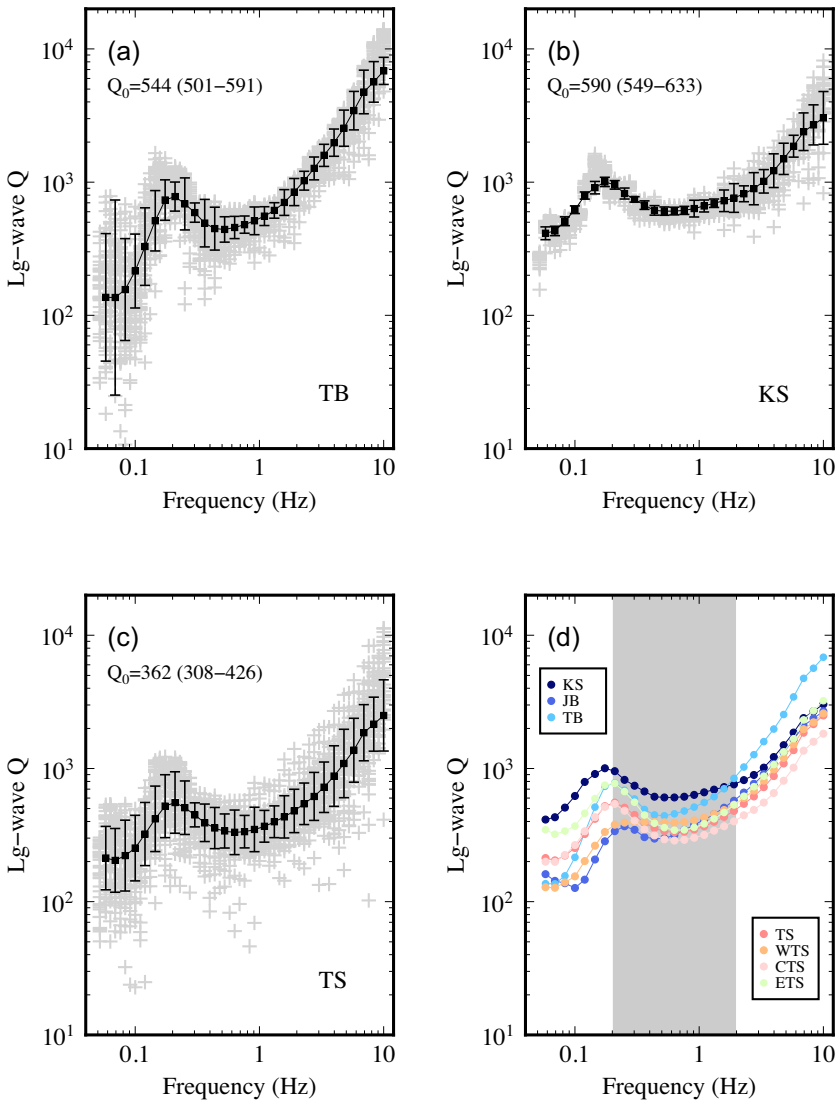

Figure 6. Frequency-dependent Lg-wave Q for different geology blocks, with (a) the Tarim Basin (TB), (b) Kazakh Shield (KS) and (c) Tien Shan (TS), respectively. Grey crosses are directly measured Q_{Lg}. Filled symbols and error bars are mean values and logarithmic standard deviations by averaging logarithmic Q_{Lg} values within each block. (d) Q_{Lg} versus frequency for different geo-blocks. The abbreviations are the same as those in Fig. 1.

4 DISCUSSION

4.1 Mantle upwelling and partial melting beneath the central Tien Shan

As a consequence of the India–Eurasia collision, the intense orogeny of the Tien Shan is commonly accepted to be directly related to the northward lithospheric underthrusting of the Tarim Basin. The geological surveys from Burtman (2015) demonstrated that the ruptures of large earthquakes on the northern margin of the Tarim Basin could be related to the northward underthrusting of the Tarim Basin. Recent local and teleseismic studies as well as Pn anisotropy studies have provided evidence for the northward subduction of the Tarim lithosphere and the possible southward subduction of the Kazakh Shield lithosphere beneath the CTS (Roecker *et al.* 1993; Xu *et al.* 2002; Lei & Zhao 2007; Li *et al.* 2009; Lei 2011; Zabelina *et al.* 2013). For example, the underthrusting of the Tarim lithosphere can be described as high-velocity anomalies dipping north in the mantle beneath the CTS (Xu *et al.* 2002; Koulakov 2011; Sychev *et al.* 2018), while the southward-dipping high-velocity anomalies may imply the subduction of the Kazakh Shield lithosphere (Li *et al.* 2009; Omuralieva *et al.* 2009; Yu *et al.* 2017). The underthrusting of the lithosphere triggers the upwelling of wet and hot underlying asthenosphere materials (Xu *et al.* 2002; Lei & Zhao 2007; Tian *et al.* 2010; Koulakov 2011; Yu *et al.* 2017). Zhou & Lei (2015) revealed a low-velocity zone in the CTS, with a significantly low Pn velocity of 7.9 km s^{-1}, suggesting a hot anomaly in the uppermost mantle due to the asthenospheric upwelling. This corresponds to the prominent strong attenuation beneath the CTS in our broad-band Lg-wave attenuation model (Fig. 7). These results suggest that the heat from the uppermost mantle can raise the temperature and even cause partial melting in the crust. This corresponds well with many previous studies, for example the observed crustal and upper mantle low-velocity anomalies (Xu *et al.* 2002; Friederich 2003; Lei & Zhao 2007; Li *et al.* 2009, 2012, 2016b; Lei 2011; Gao *et al.* 2014; Gilligan *et al.* 2014; Lü & Lei 2018; Sychev *et al.* 2018; Lü *et al.* 2019), low resistivity anomalies (Bielinski *et al.* 2003), high V_p/V_s ratios (Lei 2011) and high heat flow (Duchkov *et al.* 2001). Interestingly

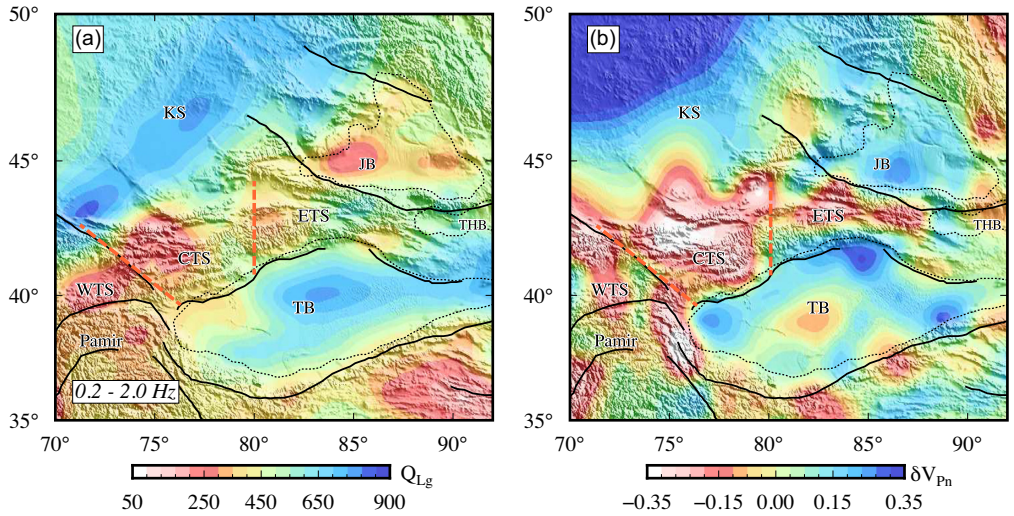

Figure 7. Comparison between (a) the average Q_{Lg} between 0.2 and 2.0 Hz and (b) the Pn velocity (Zhou & Lei 2015) in the Tien Shan and surrounding regions. The average Pn velocity is 8.2 km s^{-1}. Also shown are major faults (black lines), contours (white lines), the boundaries between WTS, CTS and ETS (red dashed lines), and the names of tectonic units (refer to Fig. 1).

, the significant strong attenuation within the crust of the CTS correlates well with its topographic boundary. The analyses of xenoliths also suggested that the mafic lower crust beneath the CTS may correspond to the underplating of upwelling mantle materials at the bottom of the crust (Zheng *et al.* 2006), implicating that mantle upwelling has reached the crust. The evidence demonstrates that the northward underthrusting of the Tarim lithosphere and the southward underthrusting of the Kazakh lithosphere may serve as key forces driving the formation and evolution of the CTS and causing large-scale partial melting within the CTS crust.

4.2 Uplift of the eastern Tien Shan due to lithosphere compression

The lateral width and elevation of the ETS are smaller than those of the CTS, and the attenuation observed in the ETS is weaker than that in the CTS, revealing the possibility of a different orogenic mechanism beneath the ETS. Zhao *et al.* (2003) performed an inversion, which jointly uses the deep seismic sounding data, and magnetotelluric and gravitational data to investigate the lithospheric cross-section from the Junggar Basin to Tarim Basin including the ETS. The result suggests that the lower crust and lithospheric mantle of the Tarim Basin subducted into the mantle of the ETS and the mass of the lower crust of the Tarim Basin was carried down to the upper mantle beneath the Tien Shan, which is probably responsible for the crustal thickening of the Tien Shan. The thickened crust is also observed by receiver functions beneath the ETS, and the uppermost mantle of the Junggar Basin has subducted southward beneath the ETS (Li *et al.* 2016a). This interpretation is also supported by body wave tomographic studies which found the lithosphere of the Tarim and Junggar Basins is asymmetrically subducted into the ETS mantle (Xu *et al.* 2002; Guo *et al.* 2006). The low-velocity anomalies widely existing in the upper mantle indicate a weak upper mantle, which could facilitate the creation of necessary conditions for accelerating the uplift and distortion of the ETS crust (Xu *et al.* 2002; Guo *et al.* 2006). Full-wave ambient noise tomography from Lü *et al.* (2019) observed a connected high-velocity upper mantle structure from the Tarim Basin across the ETS to the Junggar Basin, suggesting that the Tarim and Junggar Basins have converged and formed a barrier, which consequently prevents asthenospheric upwelling. This explanation is consistent with the relatively weak attenuation anomaly observed in the crust of ETS. Thus, we infer that the relatively weak attenuation anomalies observed within the crust of the ETS may be mainly related to fractures induced by compression between the basins and mountains rather than caused by mantle upwelling. The compression of the Tarim and Junggar lithosphere may be the dominant factor causing the uplift of the ETS. Furthermore, the GPS velocity is ∼6–9 mm yr^{-1} in the ETS, which is obviously slower than those in the WTS and CTS (Reigber *et al.* 2001), suggesting that the cold and hard Kazakh Shield revealed by pronounced high-Q_{Lg} anomalies may block the far-field effect of the India–Eurasia collision. Therefore, the Tien Shan Mountains extended toward the northeast to enter relatively weak areas.

4.3 Subduction-induced thermal anomalies in the Western Tien Shan and Pamir

Due to the strong Indo-Asian collision, the WTS and Pamir have experienced intense crustal shortening and significant crustal thickening, which is supported by GPS measurements with an approximate northward surface motion of ∼20 mm yr^{-1} (Reigber *et al.* 2001; Zubovich *et al.* 2010), possibly leading to the uplift of the whole WTS. However, the southern WTS is connected with the Pamir Plateau and characterized by low-Q_{Lg} anomalies within the crust; this connection is also supported by other geophysical anomalies, such as low-velocity anomalies in the mid-lower crust (Xu *et al.* 2002; Zabelina *et al.* 2013; Li *et al.* 2018; Sychev *et al.* 2018; Lü *et al.* 2019), high V_p/V_s ratios (Lei 2011; Sippl *et al.* 2013), high electrical conductivities (Sass *et al.* 2014) and high heat flows (Duchkov *et al.* 2001), suggesting high temperature and the occurrence of partial melting in the mid-lower crust beneath the northeastern margin of the Pamir Plateau and the southern WTS. Therefore, we consider that low-Q_{Lg} anomalies may represent partial melting within the hot and weak crust resulting from asthenospheric upwelling due to the India–Eurasia collision (Schneider *et al.* 2013; Sippl *et al.* 2013). This may indicate that the uplift of the southern WTS is related to the intrusion of mantle-derived thermal materials into the crust caused by the subduction and collision of the Indian and

Eurasian plates. In addition, a sharp velocity difference across the Talas-Fergana fault, considered a remarkable boundary between the WTS and CTS, is detected from the upper mantle to the lower crust (Roecker *et al.* 1993; Zhou & Lei 2015; Lü *et al.* 2019), which is consistent with the Q_{Lg} variations beneath the Talas-Fergana fault (Fig. 5a) and indicates that the Talas-Fergana fault may be a channel for hot material upwelling from the upper mantle.

4.4 The geodynamic mechanisms of the Tien Shan orogenic belt

Combined with other geophysical and geological observations, including seismic velocity structures, resistivity structures, crustal Poisson's ratios, seismic anisotropy, GPS velocities, seismic activity, etc., our Q_{Lg} model suggests that the three segments of the Tien Shan orogenic belt may experience complex dynamic mechanisms (e.g. Lei 2011; Lü *et al.* 2019). In view of the above-mentioned observations of the crust and upper mantle structure beneath the Tien Shan, we infer that the rapid uplift of the Tien Shan orogenic belt is caused mainly by the far-field effect of the India–Eurasia collision and that the relatively hot and weak upper mantle beneath the Tien Shan provides a necessary condition for the uplift and modification of the Tien Shan crust, which may involve crust–mantle convection leading to partial melting in the lower crust. The upwelling of hot materials may reduce the strength of the lower crust, and the buoyancy of mantle upwelling could consequently result in the uplift of the orogenic belt. However, the crustal deformation of the ETS is distinct from that of the CTS, as suggested by the pattern of Q_{Lg} distributions, indicating that mantle upwelling may be mostly related to the uplift of the CTS, whereas the uplift of the ETS is related to the subduction and compression of the lithosphere beneath the Tarim and Junggar Basins. The WTS is close to the western syntaxis of the Tibetan Plateau and affected by direct compression due to the India–Eurasia collision. The uplift of the northern WTS, which is connected with the Pamir Plateau, is further related to thermal subduction-induced upwelling and intrusion into the crust due to the collision between the Indian and Eurasian plates. In addition, the Kazakh Shield blocks the far-field effect of the India–Eurasia collision so that the Tien Shan orogenic belt extends northeastward to relatively weak areas.

5 CONCLUSION

We obtained a broad-band high-resolution attenuation model of Northwest China and surrounding areas, including the Tien Shan orogenic belt, Pamir plate, Kazakh Shield, and Tarim and Junggar Basins, using a large Lg-wave data set. The frequency band is 0.05–10.0 Hz, and the maximum resolution reaches approximately $1^\circ \times 1^\circ$ at 1.0 Hz. The model shows an apparent correlation between lateral variations in attenuation and regional tectonics. Low-Q_{Lg} anomalies are observed beneath some tectonically active regions, such as the Tien Shan orogenic belt and the northeastern margin of the Pamir Plateau, while stable geo-blocks such as the Kazakh Shield and the Tarim Basin are characterized by relatively high Q_{Lg} values. The strongest Lg-wave attenuation is observed beneath the CTS. In combination with the low seismic velocities, low resistivity anomalies and high crustal V_p/V_s ratios at depths ranging from 30 to 50 km, the low Q_{Lg} values provide new evidence for the presence of widespread melting in the crust. The high-temperature anomalies beneath the CTS are likely from mantle material upwelling due to the lithospheric underthrusting of the Tarim Basin and Kazakh Shield. Lateral variations of the Q_{Lg} values in the Tien Shan orogenic belt suggest that mantle upwelling apparent to be mostly related to the uplift and deformation of the CTS, while crustal thickening and uplift in the ETS and WTS are likely induced by lithospheric compression. In addition, strong earthquakes, low Pn velocities and relatively strong attenuation anomalies were observed within the crust in the junction between the Pamir Plateau and WTS, indicating the area may be further uplifted by the intrusion of mantle-derived thermal materials into the crust caused by the collision of the Indian and Eurasian plates and present a hot and active crust. The pronounced high-Q_{Lg} values reveal that the Kazakh Shield is a cold and hard terrane, which blocks the far-field effect of the India–Eurasia collision; hence, the Tien Shan Mountains extend northeastward to relatively weak areas.

ACKNOWLEDGMENTS

The comments from Editor G. Laske, Assistant Editor F. Storey, reviewer S. M. Mousavi and an anonymous reviewer are valuable and greatly improved this manuscript. This research was supported by the National Natural Science Foundation of China (41974061, 41974054 and U2139206) and the Special Fund of China Seismic Experimental Site (2019CSES0103).

DATA AVAILABILITY

The waveforms were collected from the China Earthquake Network Center (CENC) and the Data Management Center of the China National Seismic Network at the Institute of Geophysics, China Earthquake Administration (SEISDMC, doi: 10.7914/SN/CB; Zheng *et al.* 2010) at http://www.seisdmc.ac.cn/(last accessed July 2022) for those recorded at the China National Digital Seismic Network (CNDSN) and downloaded from the Incorporated Research Institutions for Seismology Data Management Center (IRIS-DMC) at www.iris.edu (last accessed July 2022) for recordings at the Global Seismic Network (GSN) and the International Federation of Digital Seismic Networks (FDSN) stations. The heat flow data was collected from the global heat flow database maintained by the International Heat Flow Commission (IHFC) at https://ihfc-iugg.org/products/global-heat-flow-database (Fuch *et al.* 2021). Certain figures were generated using the Generic Mapping Tools (https://forum.generic-mapping-tools.org/, last accessed July 2022; Wessel *et al.* 2013).

AUTHOR CONTRIBUTIONS

Xiao Ma: formal analysis, investigation, validation, visualization, writing – original draft, writing – review and editing; Lian-Feng Zhao: conceptualization, data curation, formal analysis, funding acquisition, methodology, project administration, resources, software, supervision, writing – review and editing; Xiao-Bi Xie: conceptualization, methodology, supervision, writing – review and editing; Xu Chang: conceptualization, supervision, writing – review and editing; Zhen-Xing Yao; conceptualization, funding acquisition, project administration, supervision.

CONFLICT OF INTEREST

The authors acknowledge that there are no conflicts of interest recorded.

REFERENCES

Abdrakhmatov, K.Y. *et al.*, 1996. Relatively recent construction of the Tien Shan inferred from GPS measurements of present-day crustal deformation rates, *Nature,* **384,** 450–453.

Aki, K., 1980. Attenuation of shear-waves in the lithosphere for frequencies from 0.05 to 25 Hz, *Phys. Earth planet. Inter.,* **21,** 50–60.

Bielinski, R.A., Park, S.K., Rybin, A., Batalev, V., Jun, S. & Sears, C., 2003. Lithospheric heterogeneity in the Kyrgyz Tien Shan imaged by magnetotelluric studies, *Geophys. Res. Lett.,* **30**(15), doi:10.1029/2003GL017455.

Bouchon, M., 1982. The complete synthesis of seismic crustal phases at regional distances, *J. geophys. Res.,* **87**(B3), 1735–1741.

Boyd, O.S., Jones, C.H. & Sheehan, A.F., 2004. Foundering lithosphere imaged beneath the Southern Sierra Nevada, California, USA, *Science,* **305,** 660–662.

Bürgmann, R. & Dresen, G., 2008. Rheology of the lower crust and upper mantle: evidence from rock mechanics, geodesy, and field observations, *Annu. Rev. Earth planet. Sci.,* **36,** 531–567.

Burtman, V.S., 1975. Structural geology of Variscan Tien Shan, USSR, *Am. J. Sci.,* **275A,** 157–186.

Burtman, V.S., 2015. Tectonics and geodynamics of the Tian Shan in the middle and late paleozoic, *Geotectonics,* **49,** 302–319.

Chen, Y.H., Roecker, S.W. & Kosarev, G.L., 1997. Elevation of the 410 km discontinuity beneath the central Tien Shan: evidence for a detached lithospheric root, *Geophys. Res. Lett.,* **24,** 1531–1534.

Chen, Y.P. *et al.*, 2005. Shear wave splitting observations in the Chinese Tianshan orogenic belt, *Geophys. Res. Lett.,* **32,** 4.

Cherie, S.G., Gao, S.S., Liu, K.H., Elsheikh, A.A., Kong, F.S., Reed, C.A. & Yang, B.B., 2016. Shear wave splitting analyses in Tian Shan: geodynamic implications of complex seismic anisotropy, *Geochem. Geophys. Geosyst.,* **17,** 1975–1989.

Craig, T.J., Copley, A. & Jackson, J., 2012. Thermal and tectonic consequences of India underthrusting Tibet, *Earth planet. Sci. Lett.,* **353,** 231–239.

De Grave, J. *et al.*, 2011. The thermo-tectonic history of the Song-Kul plateau, Kyrgyz Tien Shan: constraints by apatite and titanite thermochronometry and zircon U/Pb dating, *Gondwana Res.,* **20,** 745–763.

Duchkov, A.D., Shvartsman, Y.G. & Sokolova, L.S., 2001. Deep heat flow in the Tien Shan: advances and drawbacks, *Geol. Geofiz.,* **42,** 1516–1531.

England, P. & Molnar, P., 2015. Rheology of the lithosphere beneath the central and western Tien Shan, *J. geophys. Res.,* **120,** 3803–3823.

Fan, G.W. & Lay, T., 2002. Characteristics of lg attenuation in the Tibetan Plateau, *J. geophys. Res.,* **107,** ESE 14–11-ESE 14-15.

Friederich, W., 2003. The S-velocity structure of the East Asian mantle from inversion of shear and surface waveforms, *Geophys. J. Int.,* **153,** 88–102.

Fuch, S., Norden, B., Commission, I. & F., H., 2021. The Global Heat Flow database: release 2021, *GFZ Data Services,* doi:10.5880/fidgeo.2021.014.

Gallegos, A., Ranasinghe, N., Ni, J. & Sandvol, E., 2017. Lg attenuation, frequency dependence and relative site response of the western United States as revealed by the EarthScope Transportable Array, *Geophys. J. Int.,* **209,** 1955–1971.

Gao, X., Guo, Z., Wang, W. & Wu, Y., 2014. Crustal structure beneath the central Tien Shan from ambient noise tomography, *Terra Nova,* **26,** 469–476.

Gilligan, A., Roecker, S.W., Priestley, K.F. & Nunn, C., 2014. Shear velocity model for the Kyrgyz Tien Shan from joint inversion of receiver function and surface wave data, *Geophys. J. Int.,* **199,** 480–498.

Guo, B., Liu, Q.Y., Chen, J.H., Zhao, D.P., Li, S.C. & Lai, Y.G., 2006. Seismic tomography of the crust and upper mantle structure underneath the Chinese Tianshan, *Chin. J. Geophys.,* **49,** 1693–1700.

He, X., Zhao, L.F., Xie, X.B., Tian, X. & Yao, Z.X., 2021. Weak crust in southeast Tibetan Plateau revealed by lg-waveattenuation tomography: implications for crustal material escape, *J. geophys. Res.,* **126**(3),.

Kaban, M.K. & Yuanda, T.R., 2014. Density structure, isostatic balance and tectonic models of the central Tien Shan, *Surv. Geophys.,* **35,** 1375–1391.

Kennett, B.L.N., 1986. Lg waves and structural boundaries, *Bull. seism. Soc. Am.,* **76**(4), 1133–1141.

Kosarev, G.L., Petersen, N.V., Vinnik, L.P. & Roecker, S.W., 1993. Receiver functions for the Tien Shan Analog Broadband Network: contrasts in the evolution of structures across the Talasso-Fergana Fault, *J. geophys. Res.,* **98,** 4437–4448.

Koulakov, I., 2011. High-frequency P and S velocity anomalies in the upper mantle beneath Asia from inversion of worldwide traveltime data, *J. geophys. Res.,* **116,**

Kreemer, C., Blewitt, G. & Klein, E.C., 2014. A geodetic plate motion and global strain rate model, *Geochem. Geophys. Geosyst.,* **15,** 3849–3889.

Kumar, P., Yuan, X., Kind, R. & Kosarev, G., 2005. The lithosphere-asthenosphere boundary in the Tien Shan-Karakoram region from S receiver functions: evidence for continental subduction, *Geophys. Res. Lett.,* **32**(7),.

Laske, G., Masters, G., Ma, Z. & Pasyanos, M., 2013. Update on CRUST1.0 – a 1-degree global model of Earth's crust, in *Proceedings of the EGU General Assembly 2013,* held 7–12 April 2013 in Vienna, Austria, id. EGU2013-2658.

Lei, J., 2011. Seismic tomographic imaging of the crust and upper mantle under the central and western Tien Shan orogenic belt, *J. geophys. Res.,* **116**(B9),.

Lei, J. & Zhao, D., 2007. Teleseismic P-wave tomography and the upper mantle structure of the central Tien Shan orogenic belt, *Phys. Earth planet. Inter.,* **162,** 165–185.

Li, H., Li, S., Song, X.D., Gong, M., Li, X. & Jia, J., 2012. Crustal and uppermost mantle velocity structure beneath northwestern China from seismic ambient noise tomography, *Geophys. J. Int.,* **188,** 131–143.

Li, J.Y. *et al.*, 2016a. Mantle subduction and uplift of intracontinental mountains: a case study from the Chinese Tianshan Mountains within Eurasia, *Sci. Rep.,* **6,**.

Li, W., Chen, Y., Yuan, X.H., Schurr, B., Mechie, J., Oimahmadov, I. & Fu, B.H., 2018. Continental lithospheric subduction and intermediate-depth seismicity: constraints from S-wave velocity structures in the Pamir and Hindu Kush, *Earth planet. Sci. Lett.,* **482,** 478–489.

Li, Y., Shi, L. & Gao, J., 2016b. Lithospheric structure across the central Tien Shan constrained by gravity anomalies and joint inversions of receiver function and Rayleigh wave dispersion, *J. Asian Earth Sci.,* **124,** 191–203.

Li, Y., Wu, Q., Jiang, L. & Zhang, R., 2010. Complex seismic anisotropic structure beneath the central Tien Shan revealed by shear wave splitting analyses, *Geophys. J. Int.,* **181**(3),.

Li, Z., Roecker, S., Li, Z., Wei, B., Wang, H., Schelochkov, G. & Bragin, V., 2009. Tomographic image of the crust and upper mantle beneath the western Tien Shan from the MANAS broadband deployment: possible evidence for lithospheric delamination, *Tectonophysics,* **477,** 49–57.

Liu, X., Zhao, D. & Li, S., 2014. Seismic attenuation tomography of the Northeast Japan arc: insight into the 2011 Tohoku earthquake (Mw9.0) and subduction dynamics, *J. geophys. Res.,* **119,** 1094–1118.

Lü, Z., Gao, H., Lei, J., Yang, X., Rathnayaka, S. & Li, C., 2019. Crustal and upper mantle structure of the Tien Shan Orogenic Belt from full-wave ambient noise tomography, *J. geophys. Res.,* **124,** 3987–4000.

Lü, Z. & Lei, J., 2018. Shear-wave velocity structure beneath the central Tien Shan (NW China) from seismic ambient noise tomography, *J. Asian Earth Sci.,* **163,** 80–89.

Luo, Y., Zhao, L.-F., Ge, Z.-X., Xie, X.-B. & Yao, Z.-X., 2021. Crustal Lg-wave attenuation in Southeast Asia and its implications for regional tectonic evolution, *Geophys. J. Int.,* **226,** 1873–1884.

Ma, X., Zhao, L.-F., Xie, X.-B, He, X. & Yao, Z.-X., 2021. Regional seismic characteristics of chemical explosions on the eastern margin of the Junggar basin, Northwest China, and of historical Semipalatinsk nuclear tests, *Bull. seism. Soc. Am.,* **111,** 606–620,

Mitchell, B.J. & Hwang, H.J., 1987. Effect of low-Q sediments and crustal Q on lg attenuation in the United-States, *Bull. seism. Soc. Am.,* **77,** 1197–1210.

Molnar, P. & Ghose, S., 2000. Seismic moments of major earthquakes and the rate of shortening across the Tien Shan, *Geophys. Res. Lett.,* **27,** 2377–2380.

Molnar, P. & Tapponnier, P., 1975. Cenozoic Tectonics of Asia: effects of a continental collision: features of recent continental tectonics in Asia

can be interpreted as results of the India–Eurasia collision, *Science,* **189,** 419–426.

Omuralieva, A., Nakajima, J. & Hasegawa, A., 2009. Three-dimensional seismic velocity structure of the crust beneath the central Tien Shan, Kyrgyzstan: implications for large- and small-scale mountain building, *Tectonophysics,* **465,** 30–44.

Pasyanos, M.E., Matzel, E.M., Walter, W.R. & Rodgers, A.J., 2009. Broad-band lg attenuation modelling in the Middle East, *Geophys. J. Int.,* **177,** 1166–1176.

Phillips, W.S., Hartse, H.E. & Rutledge, J.T., 2005. Amplitude ratio tomography for regional phase Q, *Geophys. Res. Lett.,* **32**. doi:.

Reigber, C. *et al.*, 2001. New space geodetic constraints on the distribution of deformation in Central Asia, *Earth planet. Sci. Lett.,* **191,** 157–165.

Roecker, S.W., Sabitova, T.M., Vinnik, L.P., Burmakov, Y.A., Golvanov, M.I., Mamatkanova, R. & Munirova, L., 1993. 3-Dimensional elastic-wave velocity structure of the western and central Tien-Shan, *J. geophys. Res.,* **98,** 15 779–15 795.

Sass, P., Ritter, O., Ratschbacher, L., Tympel, J., Matiukov, V.E., Rybin, A.K. & Batalev, V.Y., 2014. Resistivity structure underneath the Pamir and Southern Tian Shan, *Geophys. J. Int.,* **198,** 564–579.

Schneider, F.M. *et al.*, 2013. Seismic imaging of subducting continental lower crust beneath the Pamir, *Earth planet. Sci. Lett.,* **375,** 101–112.

Sengor, A.M.C., Natalin, B.A. & Burtman, V.S., 1993. Evolution of the Altaid tectonic collage and paleozoic crustal growth in Eurasia, *Nature,* **364,** 299–307.

Sippl, C. Team, T. *et al.*, 2013. Deep burial of Asian continental crust beneath the Pamir imaged with local earthquake tomography, *Earth planet. Sci. Lett.,* **384,** 165–177.

Stolk, W., Kaban, M., Beekman, F., Tesauro, M., Mooney, W.D. & Cloetingh, S., 2013. High resolution regional crustal models from irregularly distributed data: application to Asia and adjacent areas, *Tectonophysics,* **602,** 55–68.

Sychev, I.V., Koulakov, I., Sycheva, N.A., Koptev, A., Medved, I., El Khrepy, S. & Al-Arifi, N., 2018. Collisional processes in the crust of the Northern Tien Shan inferred from velocity and attenuation tomography studies, *J. geophys. Res.,* **123,** 1752–1769.

Taylor, S., Yang., X. & Phillips, W., 2003. Bayesian lg attenuation tomography applied to eastern Asia, *Bull. seism. Soc. Am.,* **93,** 795–803.

Tian, X., Zhao, D., Zhang, H., Tian, Y. & Zhang, Z., 2010. Mantle transition zone topography and structure beneath the central Tien Shan orogenic belt, *J. geophys. Res.,* **115**. doi:.

Vinnik, L.P., Aleshin, I.M., Kaban, M.K., Kiselev, S.G., Kosarev, G.L., Oreshin, S.I. & Reigber, C., 2006. Crust and mantle of the Tien Shan from data of the receiver function tomography, *Izvest Phys. Solid Earth,* **42,** 639–651.

Vinnik, L.P., Reigber, C., Aleshin, I.M., Kosarev, G.L., Kaban, M.K., Oreshin, S.I. & Roecker, S.W., 2004. Receiver function tomography of the central Tien Shan, *Earth planet. Sci. Lett.,* **225,** 131–146.

Wei, Z., Kennett, B.L.N. & Zhao, L.-F., 2017. Lg-wave attenuation in the Australian crust, *Tectonophysics,* **717,** 413–424.

Wessel, P., Smith, W.H.F., Scharroo, R., Luis, J. & Wobbe, F., 2013. Generic mapping tools: improved version released, *EOS, Trans. Am. geophys. Un.,* **94,** 409–410.

Windley, B.F., Allen, M.B., Zhang, C., Zhao, Z.Y. & Wang, G.R., 1990. Paleozoic accretion and cenozoic redeformation of the Chinese Tien Shan Range, central Asia, *Geology,* **18,** 128–131.

Wu, R.S., Wu, X. Y. & Xie, X.B., 2007. Simulation of high-frequency wave propagation in complex crustal waveguides using generalized screen propagators, in *Advances in Wave Propagation in Heterogeneous Earth,* Vol. **48,** Elsevier Academic Press Inc.

Xiao, W., Windley, B.F., Allen, M.B. & Han, C., 2013. Paleozoic multiple accretionary and collisional tectonics of the Chinese Tianshan orogenic collage, *Gondwana Res.,* **23,** 1316–1341.

Xie, J. & Mitchell, B.J., 1990. Attenuation of multiphase surface waves in the Basin and Range province, part I: lg and lg coda, *Geophys. J. Int.,* **102,** 121–137.

Xie, J., Wu, Z., Liu, R., Schaff, D., Liu, Y. & Liang, J., 2006. Tomographic regionalization of crustal lg Q in eastern Eurasia, *Geophys. Res. Lett.,* **33**(3),.

Xie, J., 2002. Lg Q in the eastern Tibetan Plateau, *Bull. seism. Soc. Am.,* **92,** 871–876.

Xie, X.-B. & Lay, T., 1994. The excitation of lg waves by explosions: a finite-difference investigation, *Bull. seism. Soc. Am.,* **84,** 324–342.

Xu, Y., Li, Z. & Roecker, S.W., 2007. Uppermost mantle structure and its relation with seismic activity in the central Tien Shan, *Geophys. Res. Lett.,* **34**. doi:.

Xu, Y., Liu, F., Liu, J. & Chen, H., 2002. Crust and upper mantle structure beneath western China from P wave travel time tomography, *J. geophys. Res.,* **107**(B10), ESE 4–1-ESE 4-15.

Yin, A., Nie, S., Craig, P., Harrison, T.M., Ryerson, F.J., Qian, X.L. & Yang, G., 1998. Late cenozoic tectonic evolution of the southern Chinese Tian Shan, *Tectonics,* **17,** 1–27.

Yu, Y., Zhao, D. & Lei, J., 2017. Mantle transition zone discontinuities beneath the Tien Shan, *Geophys. J. Int.,* **211,** 80–92.

Zabelina, I.V., Koulakov, I.Y. & Buslov, M.M., 2013. Deep mechanisms in the Kyrgyz Tien Shan orogen (from results of seismic tomography), *Rus. Geo. Geophys.,* **54,** 695–706.

Zelt, C.A., 1998. Lateral velocity resolution from three-dimensional seismic refraction data, *Geophys. J. Int.,* **135,** 1101–1112.

Zhao, J.M., Liu, G.D., Lu, Z.X., Zhang, X.K. & Zhao, G.Z., 2003. Lithospheric structure and dynamic processes of the Tianshan orogenic belt and the Junggar basin, *Tectonophysics,* **376,** 199–239.

Zhao, L.-F. & Xie, X.-B., 2016. Strong lg-wave attenuation in the Middle East continental collision orogenic belt, *Tectonophysics,* **674,** 135–146.

Zhao, L.-F., Xie, X.-B., He, J.-K., Tian, X. & Yao, Z.-X., 2013a. Crustal flow pattern beneath the Tibetan Plateau constrained by regional lg-wave Q tomography, *Earth planet. Sci. Lett.,* **383,** 113–122.

Zhao, L.-F., Xie, X.-B., Wang, W.-M., Zhang, J.-H. & Yao, Z.-X., 2010. Seismic lg-wave Q tomography in and around Northeast China, *J. geophys. Res.,* **115**(B8),.

Zhao, L.-F., Xie, X.-B., Wang, W.-M., Zhang, J.-H. & Yao, Z.-X., 2013b. Crustal lg-wave attenuation within the North China Craton and its surrounding regions, *Geophys. J. Int.,* **195,** 513–531.

Zhao, L.F. & Mousavi, S.M., 2018. Lateral variation of crustal lg attenuation in Eastern North America, *Sci. Rep.,* **8,**.

Zheng, J.P., Griffin, W.L., O'Reilly, S.Y., Zhang, M., Liou, J.G. & Pearson, N., 2006. Granulite xenoliths and their zircons, Tuoyun, NW China: insights into southwestern Tianshan lower crust, *Precambrian Res.,* **145,** 159–181.

Zheng, X., Jiao, W., Zhang, C. & Wang, L., 2010. Short-period Rayleigh-wave group velocity tomography through ambient noise cross-correlation in Xinjiang, Northwest China, *Bull. seism. Soc. Am.,* **100,** 1350–1355.

Zhou, L., Zhao, C., Chen, Z. & Zheng, S., 2011. Amplitude tomography of lg waves in Xinjiang and its adjacent regions, *Bull. seism. Soc. Am.,* **101,** 1302–1314.

Zhou, Z. & Lei, J., 2015. Pn anisotropic tomography under the entire Tienshan orogenic belt, *J. Asian Earth Sci.,* **111,** 568–579.

Zubovich, A.V. *et al.*, 2010. GPS velocity field for the Tien Shan and surrounding regionsGPS velocity field for the Tien Shan and surrounding regions, *Tectonics,* **29**(6),.